

Nonspherical oscillations of an encapsulated magnetic microbubble

Arun Krishna B. J. and Ganesh Tamadapu†

Department of Applied Mechanics and Biomedical Engineering, Indian Institute of Technology Madras, Chennai, 600036, India.

(Received xx; revised xx; accepted xx)

This paper presents a model for nonspherical oscillations of encapsulated bubbles coated with a polymer infused with magnetic particles, developed using membrane theory for thin weakly magnetic membranes. According to this theory, only the applied magnetic field significantly contributes to the Maxwell stress and membrane is under generalized plane stress. The study focuses on axisymmetric deformations of bubbles under symmetrically arranged magnetic coils. Non-spherical oscillations of the bubble are restricted to the linear regime, with the second mode dominating within the pressure range of the stability region. The pressure-frequency stability region is computationally determined, and its variation with different material properties and applied magnetic field is analyzed. The natural frequency of each mode is estimated using boundary layer approximation. Time-series analysis of the second mode amplitude reveals a significant oscillation amplitude relative to the bubble radius. Estimation using the model indicates that the interface magnetic susceptibility and initial bubble radius enhance the amplitude of second-mode oscillations. Computational findings suggest that the applied magnetic field does not influence the stability region for exponential stability.

Key words:

1. Introduction

Encapsulated microbubbles have become essential in biomedical applications, serving as contrast agents for ultrasound imaging and as targeted drug delivery carriers. The development of innovative all-in-one drug delivery systems has garnered significant attention due to their multifunctionality, enabling the integration of therapeutic and imaging components, as well as targeting moieties, for simultaneous targeted therapy and imaging (Stride *et al.* 2009; Sciallero *et al.* 2016; Chertok & Langer 2018). Mulvana *et al.* (2012) in their work studied experimentally oscillation of bubble encapsulated with magnetic particles in presence of magnetic field. Owen *et al.* (2015) analyzed the dynamics of magnetic bubbles, assuming them to be rigid, and studied the flow conditions necessary to retain these bubbles near the vessel wall in a Poiseuille flow under an applied magnetic field. However, designing multifunctional agents that meet specific diagnostic and therapeutic requirements remains a significant challenge. This is largely due to the limited understanding of how the integration of magnetic nanoparticles within the microbubble shells influences their mechanical properties and dynamic behavior in both ultrasound imaging and drug delivery systems. Addressing these complexities is crucial

† Email address for correspondence: gt@iitm.ac.in

for the development of effective multifunctional agents. The challenge in theoretically modeling the oscillations of encapsulated magnetic microbubbles arises from the absence of magnetic monopoles, which makes the oscillations inherently axisymmetric. Non-spherical modes are not introduced as instabilities of the spherical mode; rather, they are a direct result of the applied magnetic field, which excites these modes. The nonspherical behavior of gas bubbles is well established both theoretically and experimentally. (Hao & Prosperetti 1999; Guédra *et al.* 2016; Guédra & Inserra 2018; Shaw 2006, 2009, 2017). The numerical investigation by (Shaw 2006) and (Guédra *et al.* 2016) showed that the nonlinear mode coupling is responsible for the saturation of instabilities.

There are relatively few studies focused on modeling the non-spherical oscillations of encapsulated bubbles. Tsiglifis & Pelekasis (2011) investigated the parametric stability and dynamic buckling of encapsulated bubbles, while Liu *et al.* (2012) examined the surface instability of these bubbles and analyzed how membrane surface properties influence the natural frequencies of the bubble shell. They also showed that the parametric resonance of encapsulated bubbles is similar to that of gas bubbles, with membrane effects having no significant impact on stability. However, the above models are not completely valid as they consider only linear oscillations of shape modes. Dash & Tamadapu (2024) incorporated nonlinear mode coupling and interface energy into their model, demonstrating that non-linearity also saturates instability in the case of encapsulated bubbles.

Till now, a comprehensive model for encapsulated magnetic microbubbles remains elusive. Zhao *et al.* (2022) modeled encapsulated bubbles undergoing radial oscillations in the presence of a magnetic field, while Du *et al.* (2024) extended this by incorporating translational motion along the x and y directions in addition to radial oscillations. However, these models are incomplete, as purely radial oscillations are unrealistic due to the non-radial nature of the magnetic field. Moreover, no standard models exist in the case of magnetic bubbles, analogous to the Leaky dielectric model used for encapsulated electric bubbles (Shaw *et al.* 2009; Liu *et al.* 2018) to model the magnetoelastic interface. This is primarily because interface magneto-elasticity is not yet sufficiently developed to be applied to bubble dynamics.

To model the behavior of encapsulated magnetic microbubbles, a theory for thin magneto-elastomers is essential. However, there are only a few papers on the magneto-elastic shell theory for polymer materials. A simpler approach is the membrane theory for magneto-elastomers (Barham *et al.* 2007, 2012), which neglects the bending energy of membranes. While this simplification is technically inaccurate, as bubble deformation involves changes in curvature, it can serve as a reasonable approximation due to the low thickness-to-curvature ratio of the bubble. In this paper, this membrane theory is adopted to derive mode shape equations, by considering nonlinear radial oscillations and linear shape mode oscillations. Using the approximations from (Liu *et al.* 2012), the natural frequency of the shape modes is calculated, including the magnetic effects, and stability diagram is constructed based on driving pressure amplitude and frequency to predict the model's range of validity.

The paper is organized as follows. Section 2 provides the mathematical formulation of the problem, including the membrane theory for magneto-elastomers, the kinematics of the bubble surface, magnetic field-induced forces, fluid dynamics, and the final governing equations. In Section 3, the natural frequency of the k^{th} mode is derived using the boundary layer approximation. In Section 4 A stability criterion for linear non-autonomous systems is presented to validate the computational results. Section 5 presents stability diagrams showing the relationship between driving pressure amplitude and frequency, along with their variation across different material parameters to predict the range of validity of the model. Finally, Section 6 offers a summary and conclusion.

2. Mathematical Formulation

2.1. Magneto-elastic equations

The bubble surface is encapsulated by a polymer coating infused with magnetic nanoparticles. This facilitates the translation, radial, and non-spherical oscillations of the bubble on the application of the magnetic field. In general, the strain energy density W of magneto elastomer is a function of \mathbf{F} and \mathbf{m} (Steigmann 2004). Here, \mathbf{F} is the gradient of the deformed position \mathbf{x} with respect to reference position \mathbf{X} , and \mathbf{m} is magnetization which is the magnetic moment per unit volume. For ease of analysis and the range in which the magnetic field is applied (0.5 T – 1.5 T) the interface response is assumed to be weakly magnetic. This simplifies the expression for the free energy of the interface to a sum of elastic energy and magnetic energy as

$$W = W_e(\mathbf{F}) - \frac{\mu_o \chi}{2} \mathbf{h} \cdot \mathbf{h}. \quad (2.1)$$

Here, μ_0 is permeability of free space, χ is interface susceptibility, and \mathbf{h} is induced magnetic field at the interface. This simplifies the constitutive equations of interface stresses and magnetization as

$$\boldsymbol{\sigma} = \frac{\partial W}{\partial \mathbf{F}} \mathbf{F}^T - q \mathbf{I}, \quad \mathbf{m} = -\frac{1}{\mu_o} \frac{\partial W}{\partial \mathbf{h}} = \chi \mathbf{h}. \quad (2.2)$$

In the above equation, q is constraint pressure associated with incompressibility constraint, \mathbf{F}^T is transformation of deformation gradient and \mathbf{I} is the unit tensor. The induced field can be split as

$$\mathbf{h} = \mathbf{h}_a + \mathbf{h}_s, \quad (2.3)$$

where \mathbf{h}_a is applied magnetic field and \mathbf{h}_s is self field which is the secondary field created due to the induced magnetic moment at the interface. Due to the weakly magnetic nature of the membrane, the self field can be ignored. This simplifies the divergence of pondermotive stress $\boldsymbol{\sigma}_{\text{pon}}$ which is the sum of magnetic stress $\boldsymbol{\sigma}_{\text{mag}}$ and Maxwell stress $\boldsymbol{\sigma}_{\text{max}}$ as

$$\begin{aligned} \boldsymbol{\sigma}_{\text{max}} &= \mu_0 (\mathbf{h} \otimes \mathbf{h}) - \frac{\mu_0 (\mathbf{h} \cdot \mathbf{h})}{2} \mathbf{I}, \\ \boldsymbol{\sigma}_{\text{mag}} &= \mu_0 (\mathbf{h} \otimes \mathbf{m}), \\ \nabla \cdot \boldsymbol{\sigma}_{\text{pon}} &= \mu_0 \nabla \mathbf{h} \cdot \mathbf{m} \approx \mu_0 \chi \nabla \mathbf{h}_a \cdot \mathbf{h}_a, \end{aligned} \quad (2.4)$$

where ∇ is the del operator in the current configuration. The three-dimensional magneto-elastic equation in the absence of applied body forces in the current configuration is

$$\nabla \cdot \mathbf{T} = 0, \quad \mathbf{T} = \boldsymbol{\sigma} + \boldsymbol{\sigma}_{\text{pon}}. \quad (2.5)$$

Using the expression for the divergence of pondermotive stress from (2.4) in (2.5) and transforming the interface stress to the reference configuration modifies the above equation as,

$$\bar{\nabla} \cdot \mathbf{P} + \mu_0 \chi \nabla \mathbf{h}_a \cdot \mathbf{h}_a = 0, \quad (2.6)$$

where \mathbf{P} is the first Piola stress tensor and $\bar{\nabla}$ is del operator in reference configuration. The above equation is also valid at mid surface of the membrane

$$\bar{\nabla} \cdot \mathbf{P}_s + \mu_0 \chi \nabla \mathbf{h}_a \cdot \mathbf{h}_a = 0, \quad (2.7)$$

with \mathbf{P}_s as the Piola stress evaluated at the membrane mid-surface. Due to the thinness and the very low thickness-to-radius ratio of the bubble surface, approximately $\mathcal{O}(10^{-3})$

the interface can be modeled as a membrane (Barham *et al.* 2007, 2012). Let the membrane thickness be ϵ , divergence of the first Piola stress becomes

$$\bar{\nabla} \cdot \mathbf{P}_s = \bar{\nabla}_s \cdot \mathbf{P}_s + \mathbf{P}'_s \mathbf{k}. \quad (2.8)$$

Here, $\bar{\nabla}_s$ is the two-dimensional surface gradient operator in the reference system, \mathbf{P}'_s is the differentiation of first Piola stress in the normal direction, and \mathbf{k} is normal to the reference surface. Now, expanding first Piola stress in the thickness direction,

$$\begin{aligned} \mathbf{P}^+ &= \mathbf{P}_s + \frac{\epsilon}{2} \mathbf{P}'_s, \\ \mathbf{P}^- &= \mathbf{P}_s - \frac{\epsilon}{2} \mathbf{P}'_s, \end{aligned} \quad (2.9)$$

where \mathbf{P}^\pm are the limiting value of Piola stress at the top and bottom surface, respectively, from inside, \mathbf{k}^\pm are corresponding exterior normals at top and bottom $\pm \mathbf{k}$. Adding the traction on top \mathbf{t}_a^+ and on bottom surface \mathbf{t}_a^- the following equations are obtained

$$\begin{aligned} \mathbf{P}^+ \mathbf{k}^+ &= \alpha \mathbf{t}_a^+, \\ \mathbf{P}^- \mathbf{k}^- &= \alpha \mathbf{t}_a^-, \\ \mathbf{P}^+ \mathbf{k}^+ + \mathbf{P}^- \mathbf{k}^- &= \epsilon \mathbf{P}'_s \mathbf{k}. \end{aligned} \quad (2.10)$$

Here, α is local area dilatation. Substituting the above equations in (2.7) and rewriting in the current configuration, the following membrane equation is obtained

$$\nabla_s \cdot \boldsymbol{\sigma}_s + \alpha \frac{\mathbf{t}_a^+ + \mathbf{t}_a^-}{\epsilon} + \mu_0 \nabla \mathbf{h}_a \cdot \mathbf{h}_a = 0. \quad (2.11)$$

$\boldsymbol{\sigma}_s$ is cauchy stress at mid surface of membrane. In (2.2) the expression for stress can be represented in terms of principle stretches $\lambda_i, i = 1, 2, 3$ as

$$\boldsymbol{\sigma}_s = \sum_{i=1}^3 \left(\lambda_i \frac{\partial W}{\partial \lambda_i} - q \right) \mathbf{v}_i \otimes \mathbf{v}_i, \quad (2.12)$$

and the deformation gradient as

$$\mathbf{F} = \sum_{i=1}^3 \lambda_i \mathbf{v}_i \otimes \mathbf{u}_i, \quad (2.13)$$

where \mathbf{u}_i and \mathbf{v}_i are the principle stress directions before and after the deformation and λ_i is the stretch in the corresponding principle stress direction. Incompressibility assumption of the bubble implies $\det(\mathbf{F}) = 1$, which leads to $\lambda_3 = (\lambda_1 \lambda_2)^{-1}$. A generalized plane stress condition is assumed by which stress vector component $\boldsymbol{\sigma}_s \cdot \hat{\mathbf{n}}$ normal to membrane mid-surface vanishes. This leads the mechanical part of the stress component in the normal direction to zero and the expression for the constraint pressure can be written as

$$q = \lambda_3 \frac{\partial W}{\partial \lambda_3}.$$

2.2. Kinematics of bubble surface

In this work only axisymmetric coils with uniform current distribution is considered which creates axisymmetric magnetic fields and the applied pressure is radial. Consequently, only the axisymmetric oscillations of the bubble are taken into account.

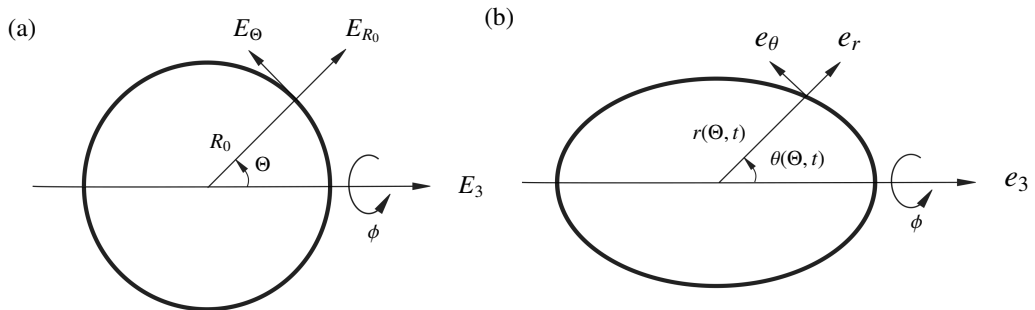


Figure 1: (a) Deformed and (b) undeformed configurations of a bubble surface.

Considering a spherical bubble of initial radius R_0 , (R_0, Θ) in the reference configuration gets transformed to (r, θ) in the current configuration as shown in Fig. 1. The position of the bubble surface after deformation is expressed in terms of the spherical mode shapes as

$$\begin{aligned}
 r(\Theta, t) &= R(t) + \sum_{k=2}^{\infty} a_k(t) P_k(\cos \Theta), \\
 \theta(\Theta, t) &= \Theta + \sum_{k=1}^{\infty} \frac{b_k(t)}{R(t)} P_k^1(\cos \Theta),
 \end{aligned}
 \tag{2.14}$$

with radial mode shape represented by the Legendre polynomial $P_k(\cos \Theta)$ and tangential mode shape represented by the associated Legendre polynomial $P_k^1(\cos \Theta)$. In (2.14) $R(t)$, $a_k(t)$ and $b_k(t)$ are deformed radius, and amplitude of radial and tangential mode shapes, respectively. The deformed and undeformed mid-surface of encapsulation are,

$$\mathbf{x} = r(\Theta, t) \cos(\phi) \sin(\theta) \mathbf{e}_1 + r(\Theta, t) \sin(\phi) \sin(\theta) \mathbf{e}_2 + r(\Theta, t) \cos(\theta) \mathbf{e}_3 = r(\Theta, t) \mathbf{e}_r,$$

$$\mathbf{X} = R_0 \cos(\phi) \sin(\Theta) \mathbf{E}_1 + R_0 \sin(\phi) \sin(\Theta) \mathbf{E}_2 + R_0 \cos(\Theta) \mathbf{E}_3 = R_0 \mathbf{E}_{R_0},
 \tag{2.15}$$

where \mathbf{E}_i and \mathbf{e}_i are the Cartesian unit basis in the undeformed and deformed interface, respectively. Additionally, \mathbf{E}_{R_0} and \mathbf{e}_r are the unit vector in the radial direction on the deformed and undeformed interface, respectively. The curvilinear basis vectors on the deformed surface are

$$\begin{aligned}
 \mathbf{g}_1 &= \mathbf{x}_{,\Theta} = r(\Theta, t)_{,\Theta} \mathbf{e}_r + r(\Theta, t) \theta_{,\Theta} \mathbf{e}_\theta, \\
 \mathbf{g}_2 &= \mathbf{x}_{,\phi} = r(\Theta, t) \sin \theta \mathbf{e}_\phi.
 \end{aligned}
 \tag{2.16}$$

The undeformed basis vectors are given by

$$\begin{aligned}
 \mathbf{G}_1 &= \mathbf{X}_{,\Theta} = R_0 \mathbf{E}_\Theta & \mathbf{G}^1 &= \frac{\mathbf{E}_\Theta}{R_0}, \\
 \mathbf{G}_2 &= \mathbf{X}_{,\phi} = R_0 \sin \phi \mathbf{E}_\phi & \mathbf{G}^2 &= \frac{\mathbf{E}_\phi}{R_0 \sin \phi},
 \end{aligned}
 \tag{2.17}$$

where the lower and upper subscripts correspond to co-variant and contra-variant vectors. The gradient on the deformed mid-surface can be written as

$$\bar{\nabla} \mathbf{x} = \mathbf{g}_\alpha \otimes \mathbf{G}^\alpha,
 \tag{2.18}$$

$$\begin{aligned}\bar{\nabla} \mathbf{x} &= \frac{r(\Theta, t)_{,\Theta}}{R_0} (\mathbf{e}_r \otimes \mathbf{E}_\theta) + \frac{r(\Theta, t)\theta_{,\Theta}}{R_0} (\mathbf{e}_\theta \otimes \mathbf{E}_\theta) + \frac{r(\Theta, t) \sin \theta}{R_0 \sin \Theta} (\mathbf{e}_\phi \otimes \mathbf{E}_\phi) \\ &= \frac{\sqrt{(r(\Theta, t)_{,\Theta})^2 + (r(\Theta, t)\theta_{,\Theta})^2}}{R_0} (\hat{\mathbf{t}} \otimes \mathbf{E}_\theta) + \frac{r(\Theta, t) \sin \theta}{R_0 \sin \Theta} (\mathbf{e}_\phi \otimes \mathbf{E}_\phi),\end{aligned}\quad (2.19)$$

$$\mathbf{F} = \bar{\nabla} \mathbf{x} + \frac{1}{\lambda_1 \lambda_2} (\hat{\mathbf{n}} \otimes \mathbf{e}_r).$$

Comparing above equations with (2.12), the principle stretches in meridional and circumferential directions become

$$\begin{aligned}\lambda_1 &= \frac{\sqrt{(r(\Theta, t)_{,\Theta})^2 + (r(\Theta, t)\theta_{,\Theta})^2}}{R_0} \approx \frac{r\theta'}{R_0} \approx \frac{R(t)}{R_0} + \frac{a_k(t)}{R_0} P_k + \frac{b_k(t)}{R_0} \frac{\partial P_k^1}{\partial \Theta}, \\ \lambda_2 &= \frac{r(\Theta, t) \sin(\theta)}{R_0 \sin(\Theta)} \approx \frac{R(t)}{R_0} + \frac{a_k(t)}{R_0} P_k + \frac{b_k(t)}{R_0} \cot(\Theta) P_k^1.\end{aligned}\quad (2.20)$$

Similarly, the normal ($\hat{\mathbf{n}}$) and the tangent ($\hat{\mathbf{t}}$) vectors on the deformed surface are

$$\begin{aligned}\hat{\mathbf{n}} &\approx \mathbf{e}_r - \frac{a_k(t)}{R(t)} P_k^1 \mathbf{e}_\theta, \\ \hat{\mathbf{t}} &\approx \mathbf{e}_\theta + \frac{a_k(t)}{R(t)} P_k^1 \mathbf{e}_r.\end{aligned}\quad (2.21)$$

From the expression for normal, the principle curvature of the deformed surface is obtained as

$$\boldsymbol{\kappa} = \nabla \hat{\mathbf{n}} = \kappa_1 \mathbf{e}_\theta \otimes \mathbf{e}_\theta + \kappa_2 \mathbf{e}_\phi \otimes \mathbf{e}_\phi, \quad (2.22)$$

where the principal curvature components κ_1 and κ_2 are given by

$$\begin{aligned}\kappa_1 &\approx \frac{1}{R(t)} - \sum_{k=2}^{\infty} \frac{a_k(t)}{R(t)^2} \left(P_k + \frac{d^2 P_k}{d\theta^2} \right), \\ \kappa_2 &\approx \frac{1}{R(t)} - \sum_{k=2}^{\infty} \frac{a_k(t)}{R(t)^2} \left(P_k + \frac{\cos(\theta)}{\sin(\theta)} P_k^1 \right).\end{aligned}\quad (2.23)$$

The membrane is assumed to follow Mooney-Rivlin constitutive law as follows

$$W_e = C_1 \left(\lambda_1^2 + \lambda_2^2 + \frac{1}{\lambda_1^2 \lambda_2^2} - 3 \right) + C_2 \left(\frac{1}{\lambda_1^2} + \frac{1}{\lambda_2^2} + \lambda_1^2 \lambda_2^2 - 3 \right). \quad (2.24)$$

The in-plane mechanical stress becomes

$$\begin{aligned}\sigma_1 &= \lambda_1 \frac{\partial W_e}{\partial \lambda_1} = 2C_1 \left(\lambda_1^2 - \frac{1}{\lambda_1^2 \lambda_2^2} \right) + 2C_2 \left(\lambda_1^2 \lambda_2^2 - \frac{1}{\lambda_1^2} \right), \\ \sigma_2 &= \lambda_2 \frac{\partial W_e}{\partial \lambda_2} = 2C_1 \left(\lambda_2^2 - \frac{1}{\lambda_2^2 \lambda_1^2} \right) + 2C_2 \left(\lambda_2^2 \lambda_1^2 - \frac{1}{\lambda_2^2} \right).\end{aligned}\quad (2.25)$$

The divergence of in-plane stress becomes (Pozrikidis 2001),

$$\begin{aligned}(\nabla \cdot \boldsymbol{\sigma})_n &= -\kappa_1 \sigma_1 - \kappa_2 \sigma_2, \\ (\nabla \cdot \boldsymbol{\sigma})_t &= \frac{\partial \sigma_1}{\partial s} + \frac{1}{d} \frac{\partial d}{\partial s} (\sigma_1 - \sigma_2),\end{aligned}\quad (2.26)$$

where d is the horizontal distance of point in membrane from axis of revolution of bubble.

$$d = R(t) \sin(\theta) + a_k(t) \sin(\theta) P_k + b_k(t) \cos(\theta) P_k^1. \quad (2.27)$$

Substituting the stretches and x in the divergence expression, we get

$$\begin{aligned} F_n^{\text{mem}} &= \frac{(\nabla \cdot \sigma_s)_n}{\lambda_1 \lambda_2} \approx \mathcal{S}_0 + \mathcal{S}_1 a_k(t) + \mathcal{S}_2 b_k(t), \\ F_t^{\text{mem}} &= \frac{(\nabla \cdot \sigma_s)_t}{\lambda_1 \lambda_2} \approx \mathcal{S}_1^1 a_k(t) + \mathcal{S}_2^1 b_k(t). \end{aligned} \quad (2.28)$$

$$\begin{aligned} \mathcal{S}_0 &= C_1 \left(\frac{-4R_0^6}{R^7} + \frac{4}{R} \right) + C_2 \left(-\frac{4R_0^4}{R^5} + \frac{4R}{R_0^2} \right), \\ \mathcal{S}_1 &= C_1 \left(-(2k^2 + 2k - 28) \frac{R_0^6}{R^8} + \frac{2k^2 + 2k - 4}{R^2} \right) \\ &\quad + C_2 \left(-(2k^2 + 2k - 20) \frac{R_0^4}{R^6} + \frac{2k^2 + 2k + 4}{R_0^2} \right), \\ \mathcal{S}_2 &= C_1 \left(-12(k^2 + k) \frac{R_0^6}{R^8} \right) + C_2 \left(-(8k^2 + 8k) \frac{R_0^4}{R^6} - \frac{4k^2 + 4k}{R_0^2} \right), \\ \mathcal{S}_1^1 &= C_1 \left(-\frac{8R_0^6}{R^8} - \frac{4}{R^2} \right) + C_2 \left(-\frac{4R_0^4}{R^6} - \frac{8}{R_0^2} \right), \\ \mathcal{S}_2^1 &= C_1 \left((4k^2 + 4k) \frac{R_0^6}{R^8} + \frac{4k^2 + 4k - 4}{R^2} \right) + C_2 \left((4k^2 + 4k - 4) \frac{R_0^4}{R^6} + \frac{4k^2 + 4k}{R_0^2} \right). \end{aligned} \quad (2.29)$$

2.3. Magnetic field and forces due to coil

Two coils are symmetrically placed above and below a bubble, each carrying current I in opposite directions and having N_1 turns. While the Biot-Savart law offers a straightforward approach to calculate the resulting magnetic field, it often involves the use of complex elliptic integrals, making the computation cumbersome. To simplify the analysis, an alternative method proposed by (Boridy 1989) is used to calculate magnetic fields for axially symmetric systems. The generalized expression for axisymmetric magnetic fields is

$$\begin{aligned} \mathbf{h}_a &= h_{ar} \mathbf{e}_r + h_{a\theta} \mathbf{e}_\theta, \\ h_{ar} &= \sum_{n=1}^{\infty} H_n \left(\frac{r}{a} \right)^{n-1} P_n(\cos \theta), \\ h_{a\theta} &= \sum_{n=1}^{\infty} \frac{H_n}{n} \left(\frac{r}{a} \right)^{n-1} P_n^1(\cos \theta), \end{aligned} \quad (2.30)$$

where r and θ are radial and angular position of any point in the $r-z$ plane. For the case of coils carrying currents in opposite direction placed symmetrically above and below the equator, the odd terms vanish in (2.30) and only even terms sustain. The expressions for even coefficients is given as below,

$$H_{2n} = -\frac{I}{a} N_1 \sin \theta_c P_{2n}^1(\cos \theta_c). \quad (2.31)$$

By choosing the value of θ_c as a positive root of P_4^1 , the co-efficient H_4 can be made zero. As we are interested in fields and field gradients in the region of the bubble, the r/a ratio is very small. Hence, the subsequent terms H_6, H_8, \dots in (2.30) can be ignored and only leading terms can be considered, resulting in simplified expressions for magnetic fields,

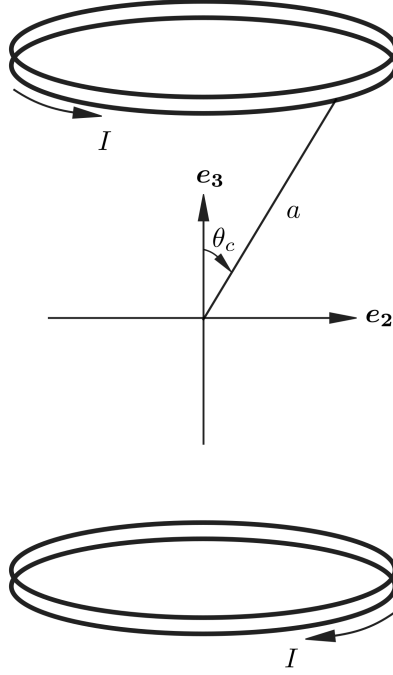


Figure 2: Two coils placed symmetrically about $e_1 - e_2$ plane carrying currents in opposite direction

as

$$\begin{aligned} h_{ar} &= H_2 \frac{r}{2a} (3 \cos^2 \theta - 1), \\ h_{a\theta} &= H_2 \frac{r}{2a} (-3 \sin \theta \cos \theta). \end{aligned} \quad (2.32)$$

In-spherical co-ordinates the magnetic forces become,

$$\begin{aligned} F_r^{mag} &= (\mu_o \chi \nabla \mathbf{h}_a \cdot \mathbf{h}_a)_r = \mu_o \chi \left(h_{ar} \frac{\partial h_{ar}}{\partial r} + \frac{h_{a\theta}}{r} \frac{\partial h_{ar}}{\partial \theta} - \frac{h_{a\theta}^2}{r} \right) \\ &= \mu_o \chi \frac{H_2^2 r}{4a^2} (3 \cos^2 \theta + 1), \\ F_\theta^{mag} &= (\mu_o \chi \nabla \mathbf{h}_a \cdot \mathbf{h}_a)_\theta = \mu_o \chi \left(h_{ar} \frac{\partial h_{a\theta}}{\partial r} + \frac{h_{a\theta}}{r} \frac{\partial h_{a\theta}}{\partial \theta} + \frac{h_{ar} h_{a\theta}}{r} \right) \\ &= \mu_o \chi \frac{H_2^2 r}{4a^2} (-3 \sin \theta \cos \theta). \end{aligned} \quad (2.33)$$

Substituting for r and θ the deformed radial and meridional position from (2.13) in the above equation we get the radial and θ component of magnetic forces. Once these components are obtained in spherical coordinates, the dot product of the magnetic forces with the normal and tangential vectors is calculated. This gives us the corresponding force

components in the normal and tangential directions as

$$\begin{aligned} F_n^{\text{mag}} &= \left(\frac{1}{\lambda_1 \lambda_2} \right) \left(F_r^{\text{mag}} - \frac{a_k(t) P_k^1}{R(t)} F_\theta^{\text{mag}} \right), \\ F_t^{\text{mag}} &= \left(\frac{1}{\lambda_1 \lambda_2} \right) \left(F_\theta^{\text{mag}} + \frac{a_k(t) P_k^1}{R(t)} F_r^{\text{mag}} \right). \end{aligned} \quad (2.34)$$

The above equations are linearized in a_k and b_k to be consistent with the present formulation. The final equations after using recurrence relations of Legendre polynomials is

$$\begin{aligned} F_n^{\text{mag}} &= \frac{H}{2R} + \frac{2H}{R^2} b_1 P_1 + \frac{H}{2R} P_2 + \frac{H}{4R^2} \left[\sum_{k=2}^{\infty} \mathcal{F}_1(k) a_k P_k + \sum_{k=2}^{\infty} \mathcal{F}_2(k) b_k P_k \right. \\ &\quad \left. + \sum_{k=0}^{\infty} \mathcal{F}_3(k) a_{k+2} P_k + \sum_{k=0}^{\infty} \mathcal{F}_4(k) b_{k+2} P_k + \sum_{k=4}^{\infty} \mathcal{F}_5(k) a_{k-2} P_k + \sum_{k=4}^{\infty} \mathcal{F}_6(k) b_{k-2} P_k \right], \\ F_t^{\text{mag}} &= -\frac{3H}{4R^2} b_1 P_1 + \frac{H}{4R} P_2 + \frac{H}{4R^2} \left[\sum_{k=2}^{\infty} \mathcal{F}_1^1(k) a_k P_k^1 + \sum_{k=2}^{\infty} \mathcal{F}_2^1(k) b_k P_k^1 \right. \\ &\quad \left. + \sum_{k=0}^{\infty} \mathcal{F}_3^1(k) a_{k+2} P_k^1 + \sum_{k=0}^{\infty} \mathcal{F}_4^1(k) b_{k+2} P_k^1 + \sum_{k=4}^{\infty} \mathcal{F}_5^1(k) a_{k-2} P_k^1 + \sum_{k=4}^{\infty} \mathcal{F}_6^1(k) b_{k-2} P_k^1 \right], \end{aligned} \quad (2.35)$$

where $H = \frac{\mu_o \chi_s H_0^2 R_0^2}{a^2}$ and $\chi_s = \epsilon \chi$. The expressions for \mathcal{F}_i and \mathcal{F}_i^1 are given Appendix A. It is evident from Liu *et al.* (2012, 2018) that applied acoustic pressure primarily excites the radial mode. If we disregard any initial disturbances to the non-spherical modes, the applied magnetic field excites the radial mode as well as the a_2 and b_2 modes. Additionally, the forcing on the k -th mode depends on the neighboring modes, specifically the $k-2$ and $k+2$ modes. As a result, under the influence of the magnetic field generated by the coil arrangement, only the even-numbered modes are triggered. This allows us to ignore the translations and odd-numbered modes in the equations for mode shapes.

2.4. Fluid equations

The assumption is made that the flow field inside the bubble is negligible and fluid flow is considered only outside the bubble, governed by the incompressible Navier–Stokes equations

$$\begin{aligned} \nabla \cdot \mathbf{u} &= 0, \\ \rho \frac{\partial \mathbf{u}}{\partial t} + \rho [\mathbf{u} \cdot \nabla] \mathbf{u} &= -\nabla p + \eta \nabla \cdot (\nabla \mathbf{u} + \nabla \mathbf{u}^T), \end{aligned} \quad (2.36)$$

where \mathbf{u} and p are fluid velocity and pressure, respectively. Here, ρ and η represent the density and viscosity of the fluid, respectively. The non-spherical oscillations are assumed to be small compared to radial oscillations, and the velocity is split into potential and viscous flow (Prosperetti 1977) as follows:

$$\mathbf{u} = \mathbf{u}_p + \mathbf{u}_v. \quad (2.37)$$

The velocity of potential flow is calculated by substituting $\eta = 0$. The generalized solution for the axisymmetric Laplace equation for incompressible flow is

$$\psi = \frac{C_0 P_0}{r} + \sum_{k=2}^{\infty} \frac{C_k P_k}{r^{k+1}}, \quad (2.38)$$

$$\mathbf{u}_p = \frac{\partial \psi}{\partial r} \mathbf{e}_r + \frac{1}{r} \frac{\partial \psi}{\partial \theta} \mathbf{e}_\theta. \quad (2.39)$$

The fluid velocity continuity at the interface in the normal direction is given by

$$\begin{aligned} S &= r - R - a_k P_k, \\ 0 &= \frac{\partial S}{\partial t} + (\nabla \psi) \cdot \nabla S. \end{aligned} \quad (2.40)$$

Expanding the terms in (2.40) gives

$$-\dot{R} + \sum_{k=2}^{\infty} -\dot{a}_k P_k - \frac{C_0}{R^2} + \frac{2C_0 a_k P_k}{R^3} - \frac{(k+1)C_k P_k}{R^{k+2}} = 0. \quad (2.41)$$

The coefficients in (2.41) are determined by using the orthogonality property of Legendre polynomials. These conditions are given by collecting

0th order coefficient:

$$\begin{aligned} \dot{R} + \frac{C_0}{R^2} &= 0, \\ C_0 &= -R^2 \dot{R}, \end{aligned} \quad (2.42)$$

k^{th} order coefficient:

$$\begin{aligned} -\dot{a}_k + \frac{2C_0 a_k}{R^3} - \frac{C_k (k+1)}{R^{k+2}} &= 0, \\ C_k &= -\frac{R^{k+2}}{k+1} \left(\dot{a}_k + \frac{2a_k \dot{R}}{R} \right). \end{aligned} \quad (2.43)$$

In the Navier-Stokes equation viscosity is substituted as zero and integrated by substituting potential flow velocity and gives pressure developed due to potential flow as

$$p_p = p_\infty - \rho \left(\frac{\partial \psi}{\partial t} + \frac{1}{2} |\nabla \psi|^2 \right), \quad (2.44)$$

The viscous correction to the potential flow is obtained by solving the linearized Navier-Stokes equation (Liu *et al.* 2012, 2018).

$$\rho \frac{\partial T_k}{\partial t} + \rho \frac{\partial}{\partial r} \left(\frac{R \dot{R}^2 T_k}{r^2} \right) - \eta \frac{\partial^2 T_k}{\partial r^2} + \eta k(k+1) r^{-2} T_k = 0. \quad (2.45)$$

The viscous velocity and viscous pressure are obtained as

$$\mathbf{u}_v = \left(\sum_{k=2}^{\infty} T_k P_k - \frac{\partial \Phi}{\partial r} \right) \mathbf{e}_r - \frac{1}{r} \frac{\partial \Phi}{\partial \theta} \mathbf{e}_\theta, \quad (2.46)$$

$$p_v = \sum_{k=1}^{\infty} k \left[\mu \frac{T_k}{R} + \frac{\rho \dot{R}}{R} \int_R^{\infty} \left[\frac{R^3}{s^3} - 1 \right] \frac{R^k}{s^k} T_k ds \right] P_k, \quad (2.47)$$

$$\begin{aligned} \Phi = \sum_{k=2}^{\infty} P_k & \left[\left(-\frac{k+1}{2k+1} \int_R^{\infty} s^{-k} T_k ds + \frac{k+1}{2k+1} \int_R^r s^{-k} T_k ds \right) r^k \right. \\ & \left. - \left(\frac{k}{2k+1} R^{2k+1} \int_R^{\infty} s^{-k} T_k ds - \frac{k}{2k+1} \int_R^r s^{k+1} T_k ds \right) r^{-(k+1)} \right]. \end{aligned} \quad (2.48)$$

The viscous stress due to this flow on the bubble surface becomes,

$$\mathbf{T}_{\text{ex}}^{\text{fluid}} = \eta (\nabla \mathbf{u} + \nabla \mathbf{u}^T). \quad (2.49)$$

The components of this flow in normal and tangential directions becomes

$$\begin{aligned} \hat{\mathbf{n}} \cdot \mathbf{T}_{\text{ex}}^{\text{fluid}} \cdot \hat{\mathbf{n}} = \frac{-4\eta \dot{R}}{R} + \sum_{k=2}^{\infty} 2\mu & \left[(k+2) \frac{\dot{a}_k}{R} - 2(k-1) \frac{\dot{R}}{R^2} a_k \right. \\ & \left. + k(k+1) R^{k-2} \int_R^{\infty} s^{-k} T_k ds \right] P_k, \end{aligned} \quad (2.50)$$

$$\hat{\mathbf{t}} \cdot \mathbf{T}_{\text{ex}}^{\text{fluid}} \cdot \hat{\mathbf{n}} = \sum_{k=2}^{\infty} 2\eta \left[\frac{k+2}{k+1} \frac{\dot{a}_k}{R} + \frac{1-k}{k+1} \frac{\dot{R} a_k}{R^2} - \frac{T_k}{2R} - R^{k-2} \int_R^{\infty} s^{-k} T_k ds \right] P_k^1. \quad (2.51)$$

2.5. Final Equations

The traction on the lower and upper surfaces of the membrane are

$$\begin{aligned} \mathbf{t}_a^+ &= -p_{\text{ex}} \hat{\mathbf{n}} + \mathbf{T}_{\text{ex}}^{\text{fluid}} \hat{\mathbf{n}}, \\ \mathbf{t}_a^- &= p_{\text{in}} \hat{\mathbf{n}}. \end{aligned} \quad (2.52)$$

Dividing (2.9) by $-\alpha$ and substituting F^{mem} , F^{mag} , \mathbf{t}_a^+ and \mathbf{t}_a^- in the governing equation stress balance at the interface, following equations are obtained:

$$\begin{aligned} F_n^{\text{mem}} + \frac{p_{\text{ex}}}{\epsilon} - \frac{p_{\text{in}}}{\epsilon} - \frac{\hat{\mathbf{n}} \cdot \mathbf{T}_{\text{ex}}^{\text{fluid}} \hat{\mathbf{n}}}{\epsilon} - F_{\text{rad}}^{\text{mag}} &= 0, \\ F_t^{\text{mem}} - \frac{\hat{\mathbf{t}} \cdot \mathbf{T}_{\text{ex}}^{\text{fluid}} \hat{\mathbf{n}}}{\epsilon} - F_{\text{tan}}^{\text{mag}} &= 0. \end{aligned} \quad (2.53)$$

From the expression for the divergence of stresses at the interface, tractions from above and below it can be observed that they are well separated in terms of Legendre or associated Legendre polynomials. The orthogonality property of these polynomials can be utilized to decompose the equation into separate modes.

$$\left. \begin{aligned} \int_{-1}^1 P_n^k P_m^k dx &= 0 \quad \text{when} \quad [m \neq n], \\ \int_{-1}^1 P_n^k P_m^k dx &= \frac{2}{2n+1} \frac{(n+m)!}{(n-m)!} \quad \text{when} \quad [m = n], \end{aligned} \right\} \quad (2.54)$$

Multiplying (2.53)₁ by P_k and integrating the equations for radial, translational and k^{th} mode shape yields the following equation

$$\rho \left(R\ddot{R} + \frac{3}{2}\dot{R}^2 \right) + p_\infty - p_{in} + 4\eta \frac{\dot{R}}{R} + F_{n0}^{\text{mem}} - \frac{H}{2R} - \frac{3H}{3R^2} [\mathcal{F}_3(0)a_2(t) + \mathcal{F}_4(0)b_2(t)] = 0, \quad (2.55)$$

$$\begin{aligned} & \rho \left(\frac{R\ddot{a}_2}{3} + \dot{R}\dot{a}_2 - \frac{\ddot{R}}{3}a_2 + \frac{2\dot{R}}{R} \int_R^\infty \left[\frac{R^3}{s^3} - 1 \right] \frac{R^2}{s^2} T_2 \, ds \right) + \frac{2\eta T_2}{R} \\ & + 2\eta \left[\frac{4\dot{a}_2}{R} + \frac{2\dot{R}a_2}{R^2} - 6 \int_R^\infty s^{-2} T_2 \, ds \right] + F_{n2}^{\text{mem}} - \frac{H}{2R} \\ & - \frac{3H}{4R^2} [\mathcal{F}_1(2)a_2(t) + \mathcal{F}_2(2)b_2(t) + \mathcal{F}_3(2)a_4(t) + \mathcal{F}_4(2)b_4(t)] = 0, \end{aligned} \quad (2.56)$$

$$\begin{aligned} & \rho \left(\frac{R\ddot{a}_k}{k+1} + \left[\frac{3\dot{R}}{k+1} + \frac{2(k+2)\eta}{\rho R} \right] \dot{a}_k + \left[\frac{-(k-1)\ddot{R}}{k+1} + \frac{4(k-1)\eta}{\rho} \frac{\dot{R}}{R^2} \right] a_k + \frac{k\eta T_k}{\rho R} \right. \\ & \left. + k \frac{\dot{R}}{R} \int_R^\infty \left[\frac{R^3}{s^3} - 1 \right] \frac{R^k}{s^k} T_k \, ds - \frac{2\eta}{\rho} k(k+1) \int_R^\infty s^{-k} T_k \, ds \right) + F_{nk}^{\text{mem}} - \frac{H}{4R^2} [\mathcal{F}_1(k)a_k(t) \\ & + \mathcal{F}_2(k)b_k(t) + \mathcal{F}_3(k)a_{k+2}(t) + \mathcal{F}_4(k)b_{k+2}(t) + \mathcal{F}_5(k)a_{k-2}(t) + \mathcal{F}_6(k)b_{k-2}(t)] = 0. \end{aligned} \quad (2.57)$$

Similarly, orthogonality conditions are used to simplify (2.53)₂ to obtain the equations for b_k as

$$\begin{aligned} & 2\eta \left[\frac{k+2}{k+1} \frac{\dot{a}_k}{R} + \frac{1-k}{k+1} \frac{\dot{R}a_k}{R^2} - \frac{T_k}{2R} - R^{k-2} \int_R^\infty s^{-k} T_k \, ds \right] + F_{tk}^{\text{mem}} - \frac{H}{4R^2} [R\delta_{k2} + \mathcal{F}_1^1(k)a_k(t) \\ & + \mathcal{F}_2^1(k)b_k(t) + \mathcal{F}_3^1(k)a_{k+2}(t) + \mathcal{F}_4^1(k)b_{k+2}(t) + \mathcal{F}_5^1(k)a_{k-2}(t) + \mathcal{F}_6^1(k)b_{k-2}(t)] = 0. \end{aligned} \quad (2.58)$$

Along with this no-slip boundary condition at the surface of the bubble in tangential direction is used

$$u_\theta = r \frac{\partial \theta}{\partial t}. \quad (2.59)$$

Substituting the deformed radial and angular positions of bubble surface from (2.13) in above equation it gets simplified as

$$\frac{-\dot{a}_k}{k+1} - \frac{2\dot{R}a_k}{(k+1)R} + R^{k-1} \int_R^\infty s^{-k} T_k \, ds = \dot{b}_k - \frac{\dot{R}b_k}{R}. \quad (2.60)$$

3. Natural Frequency

To estimate the natural frequency of magnetic bubbles the thin boundary layer approximation for acoustic streaming near a surface is used similar to the approach of Liu

similarly the first equation of (3.2) is written as

$$I \{\ddot{a}_k\} + A \{a_k\} + B \{b_k\} + A_1 \{\dot{a}_k\} + B_1 \{\dot{b}_k\} + \left\{ \begin{array}{c} -\frac{H}{2R_0} \\ \vdots \end{array} \right\} = 0. \quad (3.7)$$

where I is identity matrix, A and B are matrix obtained by linearizing R and ignoring transients in R as follows,

$$A = \begin{bmatrix} \dots & \dots & \dots & \dots & \dots & \dots & \dots & \dots & \dots \\ \vdots & -\frac{H\mathcal{F}_5(k)}{4R_0^2} & 0 & \mathcal{S}_1(k) - \frac{H\mathcal{F}_1(k)}{4R_0^2} & 0 & -\frac{H\mathcal{F}_3(k)}{4R_0^2} & 0 & 0 & \vdots \\ \vdots & 0 & -\frac{H\mathcal{F}_5(k+1)}{4R_0^2} & 0 & \mathcal{S}_1(k+1) - \frac{H\mathcal{F}_1(k+1)}{4R_0^2} & 0 & -\frac{H\mathcal{F}_3(k+1)}{4R_0^2} & 0 & \vdots \\ \dots & \dots & \dots & \dots & \dots & \dots & \dots & \dots & \dots \end{bmatrix}, \quad (3.8)$$

$$B = \begin{bmatrix} \dots & \dots & \dots & \dots & \dots & \dots & \dots & \dots & \dots \\ \vdots & -\frac{H\mathcal{F}_6(k)}{4R_0^2} & 0 & \mathcal{S}_2(k) - \frac{H\mathcal{F}_2(k)}{4R_0^2} & 0 & -\frac{H\mathcal{F}_4(k)}{4R_0^2} & 0 & 0 & \vdots \\ \vdots & 0 & -\frac{H\mathcal{F}_6(k+1)}{4R_0^2} & 0 & \mathcal{S}_2(k+1) - \frac{H\mathcal{F}_2(k+1)}{4R_0^2} & 0 & -\frac{H\mathcal{F}_4(k+1)}{4R_0^2} & 0 & \vdots \\ \dots & \dots & \dots & \dots & \dots & \dots & \dots & \dots & \dots \end{bmatrix}. \quad (3.9)$$

The expression for natural frequency becomes,

$$\{\omega_k^2\} = \text{diag} \{A - BB_a^{-1}A_a\}. \quad (3.10)$$

4. Stability analysis

Analyzing the stability of (2.55), (2.57) and (2.58) is in general very difficult as they are inhomogeneous coupled system of nonlinear ODEs. There are no general approaches to understand the stability of inhomogeneous equations. Considering the system of linear coupled equations

$$\dot{\mathbf{x}} = \mathbf{A}(t)\mathbf{x} + \mathbf{f}(t), \quad (4.1)$$

where \mathbf{x} is n dimensional vector and $\mathbf{A}(t)$ is $n \times n$ matrix. If the time period of both $\mathbf{A}(t)$ and $\mathbf{f}(t)$ are same,

$$\begin{aligned} \mathbf{A}(t) &= \mathbf{A}(t+T), \\ \mathbf{f}(t) &= \mathbf{f}(t+T), \end{aligned} \quad (4.2)$$

then from the theorem proved in [Slane & Tragesser \(2011\)](#) for exponential stability of (4.1) depends only on fundamental matrix $\mathbf{X}(T)$ of homogeneous part of the system of equations. The fundamental matrix can be constructed by integrating the system of equations (4.1) till time period T with initial conditions $\mathbf{X}(0) = \mathbf{I}$. The eigenvalues of the fundamental matrix determine the stability as follows,

- Case 1: If all the eigenvalues are less than one then the system of equations is asymptotically stable.
- Case 2: If at least one eigenvalue is greater than one then the system of equations is asymptotically unstable.
- Case 3: If some eigenvalues are equal to one and the remaining is less than one, then the solution is stable but not asymptotically stable.

The system of equations for radial and tangential shape modes is not of the form (4.1). However, substituting for \ddot{R} in (2.57) from (2.55) and linearize radius as,

$$R(t) = R_0(1 + r(t)),$$

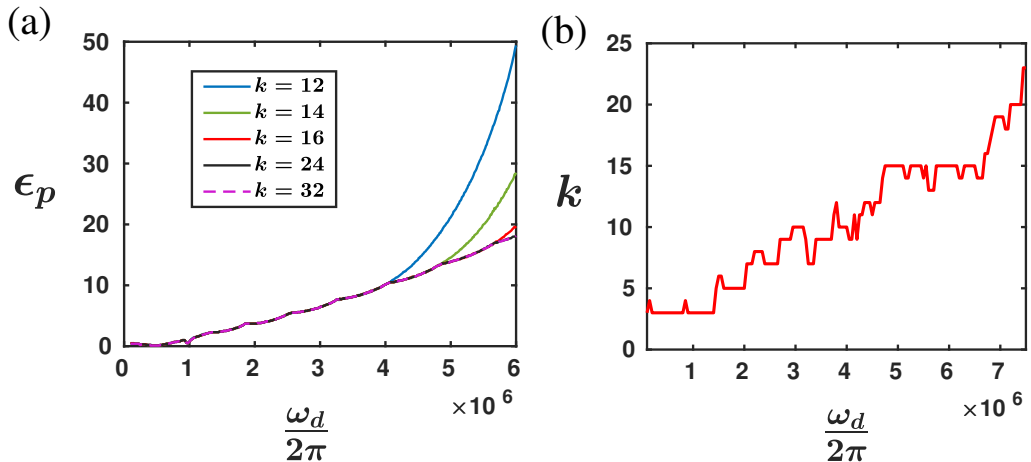


Figure 3: Convergence of stability diagram with number of modes and results of linear stability analysis. (a) Stability diagram with total modes considered in the analysis and (b) Mode number unstable at a particular frequency.

by ignoring ra_k , $r\dot{a}_k$, rb_k and $r\dot{b}_k$ as small quantities, the system of equations of bubble can be rewritten in the form of (4.1). Now the only time-dependent term in the coefficient matrix is p_∞ which is also the only time-dependent forcing term and if they are periodic then the above stability analysis holds.

5. Numerical Results and Discussion

The equations (2.55), (2.57) and (2.58), are solved using the Runge-Kutta method implemented by MATLAB ode45 package, while equation (2.45) is solved using finite difference method. The problem is approached using a one-way coupling method. At each time step t , the Runge-Kutta method is used to solve the equations, with the value of T_k at the previous time step $t-1$ being utilized. This gives the solution for the variables of interest at time t . Subsequently, the values of R , a_k , and b_k at time t are used to solve the finite difference equation, which updates the fluid terms for the current time step. The initial conditions are $R = R_0$, $a_k = 0$ and $b_k = 0$ for simulations.

5.1. Stability diagrams

In the study of bubble dynamics under an applied magnetic field, all even-numbered shape modes are excited, making it challenging to determine the number of modes need to be considered for analysis. To address this challenge, the pressure-frequency stability diagram (see figure 3(a)) is analyzed as a function of the number of modes, while applying pressure at infinity as $p_\infty = p_0(1 + \epsilon_p \cos \omega_d t)$. Here, ϵ_p and ω_d represent dimensionless acoustic pressure and circular frequency, respectively. The stability curve represents the critical pressure above which the amplitude response of at least one nonspherical mode a_k changes its behavior from bounded oscillations to exponential blowup. In the simulations, the coils are assumed to carry a current of $I = 100$ kA, with the number of coil turns set to $N_1 = 1000$, a thickness of $\epsilon = 20$ nm, and an initial bubble radius of $R_0 = 10$ μm .

Figure 3a shows that as the number of modes increases from 12 to 32, the critical pressure curves in the $\epsilon_p - \omega_d$ plane stabilize, defining a well-converged stable region where the linearized non-spherical oscillation equations remain valid. This convergence

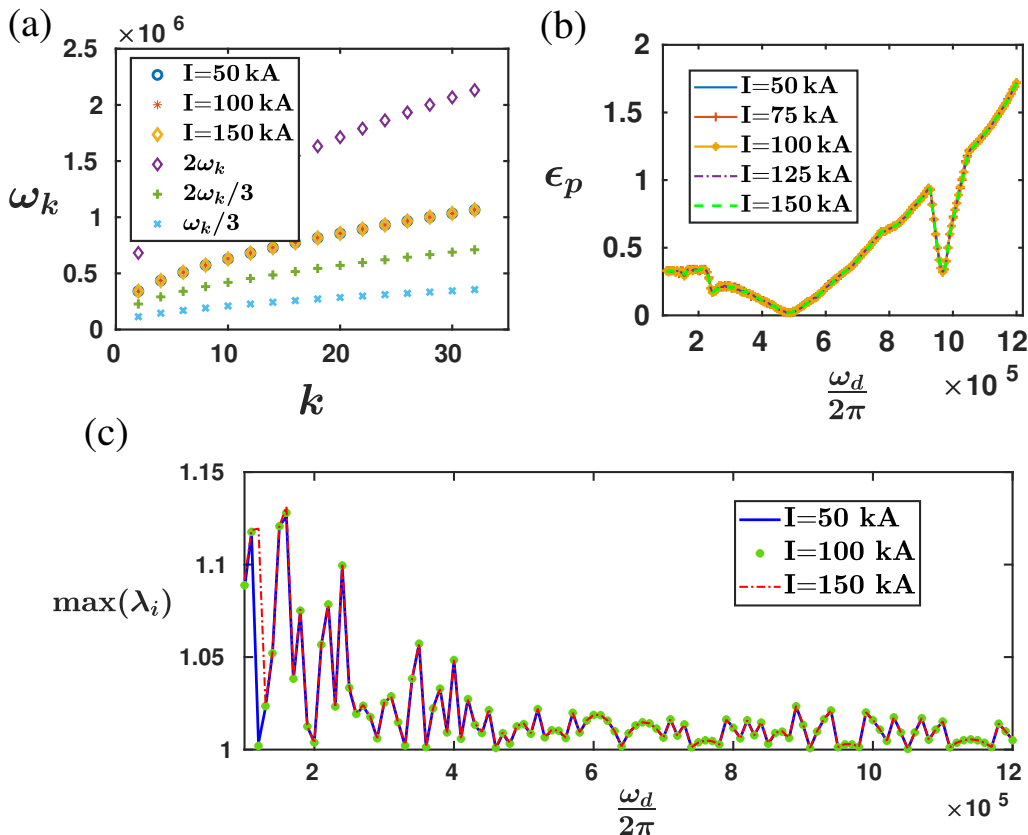


Figure 4: (a) Variation of natural frequency with mode numbers plot ω_k vs k at various values of applied current, (b) The critical pressure curves in pressure frequency plane ϵ_p vs ω_d shown for different values of applied current (c) Maximum eigenvalue of fundamental matrix variation with driving frequency at various values of applied current.

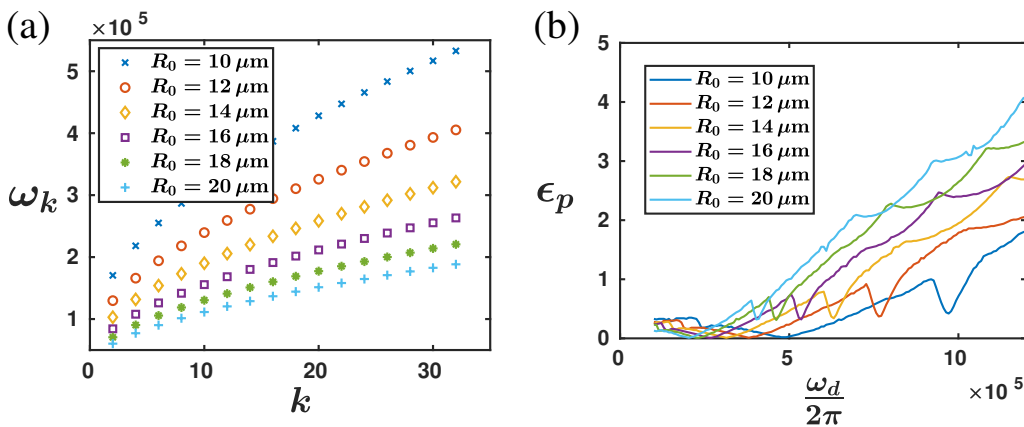


Figure 5: (a) Variation of natural frequency with mode numbers for shear modulus $c_1 = 0.1 \text{ N m}^{-1}$ and (b) critical pressure versus driving frequency curve for shear modulus $c_1 = 0.1 \text{ N m}^{-1}$ in ϵ_p vs ω_d plane shown for different values of initial radius.

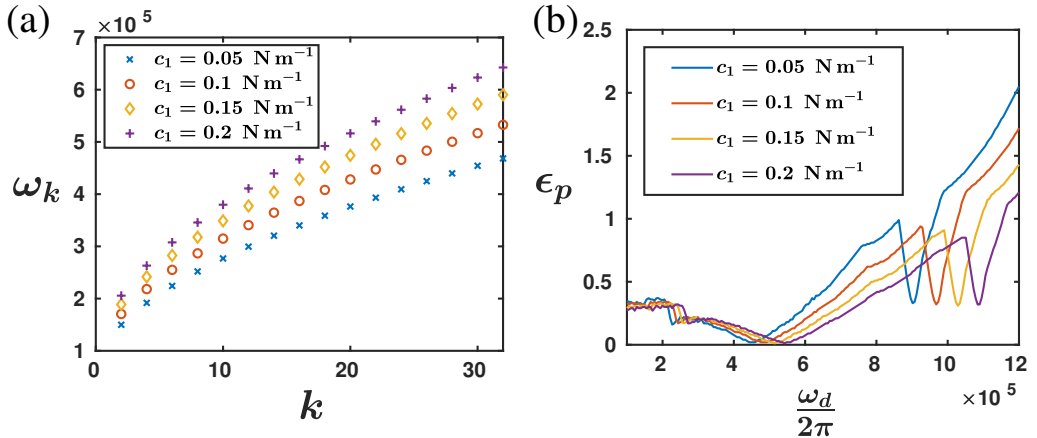


Figure 6: Plots for an undeformed bubble radius $R_0 = 10 \mu\text{m}$ with different values of surface encapsulation shear modulus c_1 . (a) Variation of natural frequency with mode numbers. (b) Critical excitation pressure (ϵ_p) versus driving frequency (ω_d) curves representing the stability boundaries.

occurs because, in the absence of initial disturbances in the shape modes, the a_2 mode is initially dominant. The amplitude of each successive even-numbered mode gradually decreases, approaching zero at higher mode numbers.

Furthermore, the stability analysis results discussed in Section 4 indicate that the first mode to become unstable during a frequency sweep shifts to higher modes as frequency increases, as shown in figure 3b. This explains the convergence of critical pressure curve when more than 16 modes are considered for driving frequencies up to 6 MHz.

5.1.1. Effect of current and material parameters on stability diagram

Figure 4b shows the influence of applied current on the critical pressure above which mode amplitude response becomes unstable. From this, it is evident that the applied magnetic field does not affect the stability diagram of surface instability. Similarly, the $\omega_k - k$ plot in figure 4a which shows the relationship between natural frequency and mode number, suggests that the applied current does not noticeably influence the natural frequency. Additionally, the same plot reveals that several harmonics, sub-harmonics, and super-harmonics of different modes are closely spaced around the fundamental frequency of a particular mode. As a result, when the critical pressure is exceeded, multiple modes become unstable simultaneously. This complexity makes stability analysis feasible only through computational methods.

Figure 4c is obtained by calculating the maximum eigenvalue of fundamental matrix $X(T)$ by varying pressure amplitude until eigenvalue becomes greater than 1. The $\max(\lambda_i)$ plot of figure 4c indicates that the maximum eigenvalue remains unaffected by increasing current in the system of equations, which explains the invariance of the stability diagram with respect to variations in current. Furthermore, figure 5 demonstrates that increasing the bubble radius while keeping other parameters constant lowers the natural frequency, shifting the stability diagram to the left. Also, from figure 6a increasing c_1 increases the natural frequency which is consistent with minima in critical pressure curves shown in figure 6b occurring at higher frequency. The slight shift of critical pressure curve down in the same plot can be explained by inspecting first equation of (3.3) where \mathcal{S}_1

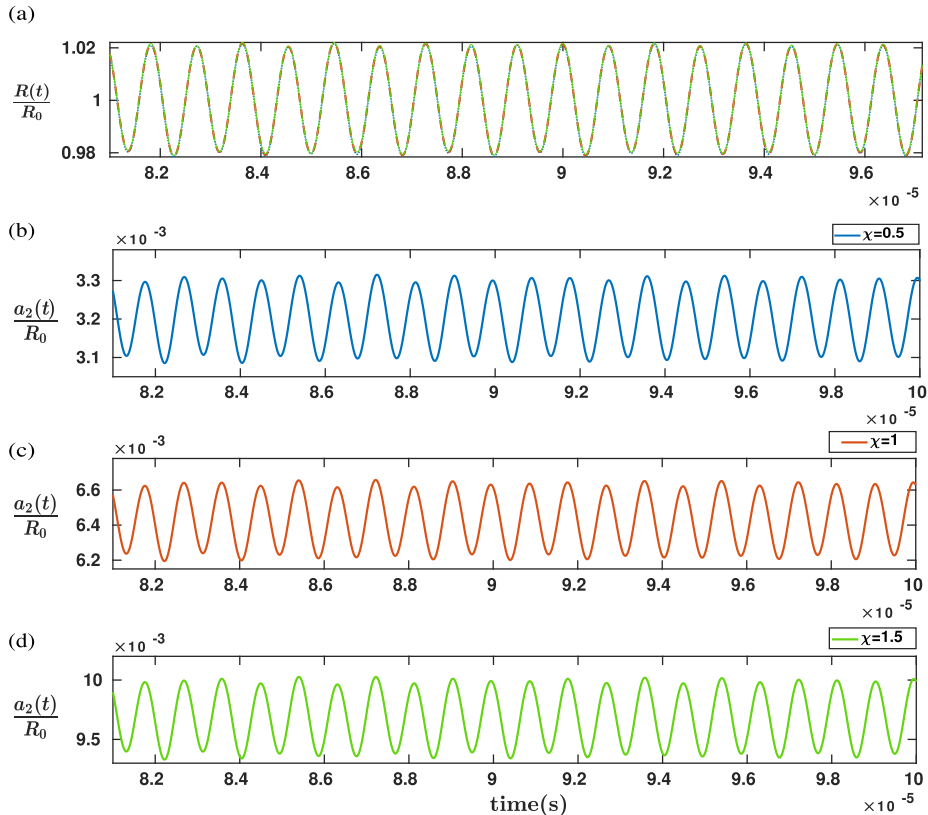


Figure 7: Variation of radial mode amplitude $R(t)$ and second mode amplitude $a_2(t)$ with time for a bubble of initial radius $R_0 = 10 \mu\text{m}$ at various values of encapsulation susceptibility. The simulations are conducted at $\omega_d = 1 \text{ MHz}$ and $\epsilon_p = 0.5$.

contains c_1 and \ddot{R} contains $-\epsilon_p$. So, lower pressure amplitude ϵ_p is enough to cause exponential blow up at higher c_1 .

5.2. Time-series of mode shapes

Radial and shape oscillations are analyzed only within the stable region of the $\epsilon_p - \omega_d$ plane. In this stable zone, the dynamics is predominantly governed by $R(t)$ and $a_2(t)$. The behavior of these two modes is studied as material properties vary. To investigate the influence of different material properties on the time series of radial and shape modes, the governing equations are non-dimensionalized. This is done by introducing the transformations:

$$R(t) = R_0 \bar{R}(t), a_k = R_0 \bar{a}_k(t), t = \sqrt{\frac{\rho_f R_0^3}{2c_1}} \bar{t},$$

where $c_1 = \epsilon C_1$ and $c_2 = \epsilon C_2$. These transformations lead to the introduction of key non-dimensional quantities: Reynolds number $Re = \sqrt{2\rho_f c_1 R_0 / \eta^2}$, which compares elastic and viscous forces in liquid, non-dimensional magnetic force parameter $Rn = \frac{\mu_o \chi H_0^2 R_0^2}{2c_1 a^2}$, strain stiffening parameter $\alpha = c_2 / c_1$ and non-dimensional pressure $P = \frac{p_0 R_0}{c_1}$. These non-dimensional parameters facilitate a systematic exploration of how material properties influence the dynamics of the system.

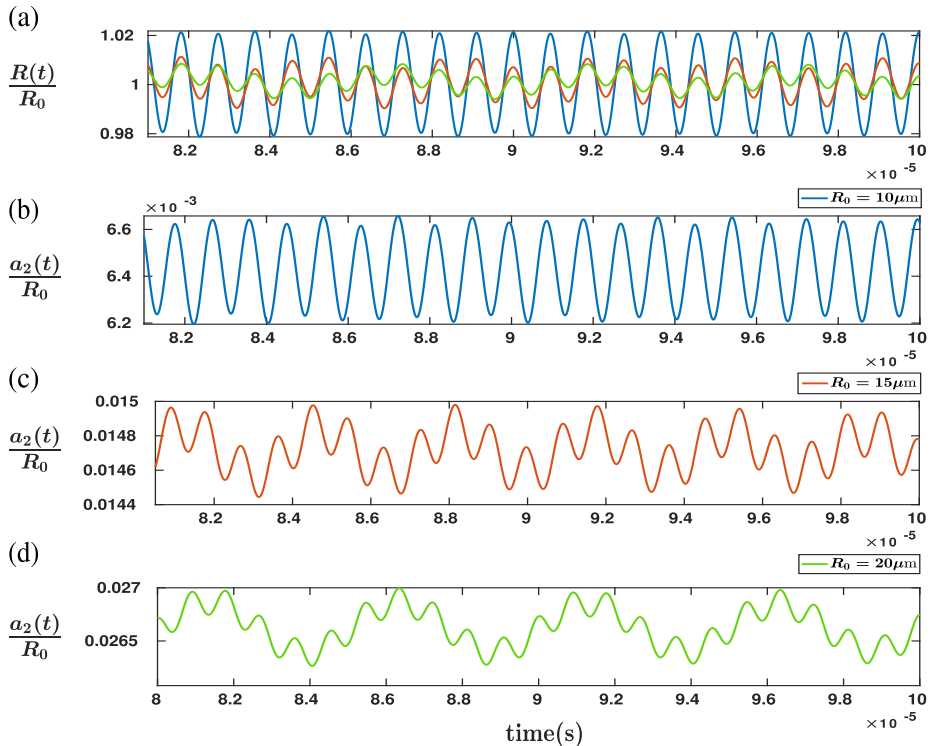


Figure 8: Variation of radial mode amplitude $R(t)$ and second mode amplitude $a_2(t)$ with time for a bubble encapsulation of susceptibility $\chi = 1$ at different values of undeformed bubble radius R_0 . The simulations are conducted at $\omega_d = 1$ MHz and $\epsilon_p = 0.5$.

5.2.1. Variation with magnetic susceptibility

Simulations are conducted with the following parameters: $R_0 = 10 \mu\text{m}$, $c_1 = 0.1 \text{ N m}^{-1}$, $c_2 = 0.12 \text{ N m}^{-1}$, $N_1 = 1000$ turns, $\epsilon = 20 \text{ nm}$, $\omega_d = 1$ MHz, $\epsilon_p = 0.5$ and $I = 100 \text{ kA}$ over a duration of $100 \mu\text{s}$. The time-dependent behavior of the radial mode and the a_2 shape mode is analyzed. The results show that the radial mode remains largely unaffected, which can be explained by the relative magnitudes of the non-dimensional forces involved. The non-dimensional pressure force, P scales as $\mathcal{O}(R_0)$ whereas non-dimensional magnetic force Rn scales as $\mathcal{O}(R_0^2)$. Since $R_0 \ll 1$, the magnetic forces are significantly smaller compared to the applied pressure, rendering their influence negligible on increasing χ . However, for the a_2 shape mode, magnetic force serves as the primary driving term, significantly influencing its maximum oscillation amplitude. This dependence on susceptibility is clearly observed, as illustrated in figure 7.

5.2.2. Variation with undeformed radius

Simulations are conducted with $c_1 = 0.1 \text{ N m}^{-1}$, $c_2 = 0.12 \text{ N m}^{-1}$, $\chi = 1$, $\epsilon = 20 \text{ nm}$, $\omega_d = 1$ MHz, $\epsilon_p = 0.5$ and $I = 100 \text{ kA}$ over a duration of $100 \mu\text{s}$. From the expressions for the non-dimensional magnetic force, it is evident that the forcing on shape modes increases with an increase in radius. Additionally, as shown in (2.55), the pressure acting on the radial mode opposes the radial motion, which leads to a reduction in the amplitude of radial oscillations with increasing radius. This behavior is clearly depicted in figure 8.

6. Summary and Conclusions

In this paper, governing equations are derived for the non-spherical oscillations of an encapsulated magnetic microbubble using a membrane approximation of weakly magnetic hyper-elastic materials. The mode shape oscillations are analyzed under the influence of time-varying pressure and a pair of oppositely directed current-carrying coils. We investigate the influence of the applied current on the stability diagram and numerically find that it does not affect stability, a conclusion further supported by stability analysis. Additionally, the effects of bubble radius, magnetic susceptibility, and shear modulus on the stability diagram and time-series data are explored.

Using the viscous penetration depth assumption for a toroidal vortex and an order-of-magnitude analysis, we formulate a method to calculate the natural frequency of shape modes. Variations in material properties are shown to cause shifts in the stability diagram, reflected in the calculated natural frequency. However, the model has notable limitations. The membrane approximation is valid primarily for slightly larger bubbles; for smaller bubbles, a shell theory would provide a more accurate approximation. Furthermore, as we focus on linear shape mode oscillations, the derived equations are only valid within a limited stable region. Beyond this region, the equations exhibit exponential divergence. Incorporating non-linear terms for shape oscillations could potentially address this divergence and lead to stabilization.

Despite these limitations, this work lays a foundational framework for studying non-spherical oscillations of encapsulated magnetic bubbles, offering a basis for further advancements in the field.

Acknowledgement. AKB would like to thank Shaik Nadeem Karim for useful discussions. AKB and GT acknowledge the Ministry of Education (MoE), Government of India, for providing research support.

Funding. This work was supported by the Science and Engineering Research Board, Department of Science and Technology, Government of India, under Project No. CRG/2022/005775.

Declaration of Interests. The authors report no conflict of interest.

Appendix A. Magnetic forces coefficients

$$\mathcal{F}_1 = \frac{-5k(k+1)}{(2k-1)(2k+3)} \quad \mathcal{F}_1^1 = \frac{3(2k^2+2k-1)}{(2k-1)(2k+3)} \quad (\text{A } 1)$$

$$\mathcal{F}_2 = \frac{10k^2(k^2+2k+1)}{(2k-1)(2k+3)} \quad \mathcal{F}_2^1 = \frac{3(k^2+k+3)}{(2k-1)(2k+3)} \quad (\text{A } 2)$$

$$\mathcal{F}_3 = \frac{-3(k+4)(k+2)(k+1)}{(2k+3)(2k+5)} \quad \mathcal{F}_3^1 = \frac{3(k^2+4k+4)}{(2k+3)(2k+5)} \quad (\text{A } 3)$$

$$\mathcal{F}_4 = \frac{3(k+1)(k+2)(k+3)(k+4)}{(2k+3)(2k+5)} \quad \mathcal{F}_4^1 = \frac{-3(k+2)(k+3)(k+4)}{(2k+3)(2k+5)} \quad (\text{A } 4)$$

$$\mathcal{F}_5 = \frac{-3k(k-1)^2}{(2k-1)(2k-3)} \quad \mathcal{F}_5^1 = \frac{3(k-1)^2}{(2k-1)(2k-3)} \quad (\text{A } 5)$$

$$\mathcal{F}_6 = \frac{3k^2(k-2)(k-1)}{(2k-1)(2k-3)} \quad \mathcal{F}_6^1 = \frac{-3(k-1)(k-2)(k-3)}{(2k-1)(2k-3)} \quad (\text{A } 6)$$

REFERENCES

- BARHAM, M, STEIGMANN, DJ, MCELFFRESH, M & RUDD, RE 2007 Finite deformation of a pressurized magnetoelastic membrane in a stationary dipole field. *Acta Mechanica* **191** (1), 1–19.
- BARHAM, M, STEIGMANN, DJ & WHITE, DAN 2012 Magnetoelasticity of highly deformable thin films: theory and simulation. *International Journal of Non-Linear Mechanics* **47** (2), 185–196.
- BORIDY, ELIE 1989 Magnetic fields generated by axially symmetric systems. *Journal of Applied Physics* **66** (12), 5691–5701.
- CHERTOK, BEATA & LANGER, ROBERT 2018 Circulating magnetic microbubbles for localized real-time control of drug delivery by ultrasonography-guided magnetic targeting and ultrasound. *Theranostics* **8** (2), 341.
- DASH, NEHAL & TAMADAPU, GANESH 2024 Nonspherical oscillations of an encapsulated microbubble with interface energy under the acoustic field. *The Journal of the Acoustical Society of America* **155** (4), 2445–2459.
- DU, ZHIWEI, PAN, RUIQI, LI, FAN, MO, RUNYANG & WANG, CHENGHUI 2024 Local control of magnetic microbubble behavior by magnetic field and pulsed ultrasound. *Applied Acoustics* **216**, 109792.
- GUÉDRA, MATTHIEU & INSERRA, CLAUDE 2018 Bubble shape oscillations of finite amplitude. *Journal of Fluid Mechanics* **857**, 681–703.
- GUÉDRA, MATTHIEU, INSERRA, CLAUDE, MAUGER, CYRIL & GILLES, BRUNO 2016 Experimental evidence of nonlinear mode coupling between spherical and nonspherical oscillations of microbubbles. *Physical Review E* **94** (5), 053115.
- HAO, YUE & PROSPERETTI, ANDREA 1999 The effect of viscosity on the spherical stability of oscillating gas bubbles. *Physics of Fluids* **11** (6), 1309–1317.
- LIU, YUNQIAO, HE, DONGDONG, GONG, XIAOBO & HUANG, HUAXIONG 2018 Deformation of an encapsulated bubble in steady and oscillatory electric fields. *Journal of Fluid Mechanics* **844**, 567–596.
- LIU, YUNQIAO, SUGIYAMA, KAZUYASU, TAKAGI, SHU & MATSUMOTO, YOICHIRO 2012 Surface instability of an encapsulated bubble induced by an ultrasonic pressure wave. *Journal of Fluid Mechanics* **691**, 315–340.
- MULVANA, HELEN, ECKERSLEY, ROBERT J, TANG, MENG-XING, PANKHURST, QUENTIN & STRIDE, ELEANOR 2012 Theoretical and experimental characterisation of magnetic microbubbles. *Ultrasound in Medicine & Biology* **38** (5), 864–875.
- OWEN, JOSHUA, RADEMEYER, PAUL, CHUNG, DANIEL, CHENG, QIAN, HOLROYD, DAVID, COUSSIOS, CONSTANTIN, FRIEND, PETER, PANKHURST, QUENTIN A & STRIDE, ELEANOR 2015 Magnetic targeting of microbubbles against physiologically relevant flow conditions. *Interface Focus* **5** (5), 20150001.
- POZRIKIDIS, C 2001 Effect of membrane bending stiffness on the deformation of capsules in simple shear flow. *Journal of Fluid Mechanics* **440**, 269–291.
- PROSPERETTI, ANDREA 1977 Viscous effects on perturbed spherical flows. *Quarterly of Applied Mathematics* **34** (4), 339–352.
- SCIALLERO, CLAUDIA, BALBI, LUCA, PARADOSSI, GAIO & TRUCCO, ANDREA 2016 Magnetic resonance and ultrasound contrast imaging of polymer-shelled microbubbles loaded with iron oxide nanoparticles. *Royal Society Open Science* **3** (8), 160063.
- SHAW, SJ 2006 Translation and oscillation of a bubble under axisymmetric deformation. *Physics of Fluids* **18** (7), 072104.
- SHAW, SJ 2009 The stability of a bubble in a weakly viscous liquid subject to an acoustic traveling wave. *Physics of Fluids* **21** (2), 022104.

- SHAW, SJ 2017 Nonspherical sub-millimeter gas bubble oscillations: Parametric forcing and nonlinear shape mode coupling. *Physics of Fluids* **29** (12).
- SHAW, SJ, SPELT, PDM & MATAR, OK 2009 Electrically induced bubble deformation, translation and collapse. *Journal of Engineering Mathematics* **65**, 291–310.
- SLANE, JEAN & TRAGESSE, STEVEN 2011 Analysis of periodic nonautonomous inhomogeneous systems. *Nonlinear Dynamics and Systems Theory* **11** (2), 183–198.
- STEIGMANN, DJ 2004 Equilibrium theory for magnetic elastomers and magnetoelastic membranes. *International Journal of Non-Linear Mechanics* **39** (7), 1193–1216.
- STRIDE, ELEANOR, PORTER, COLIN, PRIETO, ANA GARCIA & PANKHURST, QUENTIN 2009 Enhancement of microbubble mediated gene delivery by simultaneous exposure to ultrasonic and magnetic fields. *Ultrasound in Medicine & Biology* **35** (5), 861–868.
- TSIGLIFIS, KOSTAS & PELEKASIS, NIKOS A 2011 Parametric stability and dynamic buckling of an encapsulated microbubble subject to acoustic disturbances. *Physics of Fluids* **23** (1).
- ZHAO, LIXIA, SHI, HUIMIN, BELLO, ISAAC, HU, JING, WANG, CHENGHUI & MO, RUNYANG 2022 Nonlinear oscillation characteristics of magnetic microbubbles under acoustic and magnetic fields. *Chinese Physics B* **31** (3), 034302.